Study of Physical Mechanism of Two-color Laser Field Pumped THz Wave in Air Plasma

Shengqi Xu, Yizhu Zhang, Yinbo Zheng, Weiwei Liu *
Institute of Modern Optics, Nankai University,
Key Laboratory of Opto-electronic Information Science and Technology,
Education Ministry of China, Tianjin 300071, P.R. China
* Email: liuweiwei@nankai.edu.cn

(Received 8 December 2009; accepted 3 August 2010)

Abstract: THz wave generation during the laser-air interaction is investigated both experimentally and theoretically. The pump laser is a combination of a femtosecond Ti:sapphire laser pulse and its second harmonic. The polarization of the generated THz wave is experimentally measured. Comparison study has been carried out theoretically between the free electron drifting current model and the macroscopic four-wave mixing model. The result indicates that the four-wave mixing model could give better description to the experimental observations rather than the free electron drifting current model.

Keywords: Femtosecond laser, terahertz generation, four-wave mixing

doi: 10.11906/TST.130-142.2010.09.13

1. Introduction

THz wave generation by femtosecond laser pulse in self-generated air plasma has received extensive research interests. Especially, by combining a near-infrared femtosecond laser pulse and its second harmonic, the efficiency of the THz generation could be significantly enhanced [1-6]. The simplicity of the experimental setup and the high peak power of the resulted THz pulse have made this so-called two-color laser pumping method a competitive THz source for various potential applications, such as stand-alone THz remote-sensing and nonlinear THz spectroscopy. However, the interpretation about the underlying physical mechanism of the THz generation by a two-color laser field in air plasma remains controversial.

In the single pulse case, the THz generation is attributed to spatial unhomogeneous distribution of free electron ponderomotive energy in the relativistic regime [7] or four-wave mixing (4*WM*) in ambient air [8], respectively. When two-color laser field was implemented, Kress et al. first suggested that THz wave is given rise by four-wave mixing process from the macroscopic point of view, while Kim et al. have highlighted the free electron drifting current (EC) model. Under the framework of four-wave mixing theory, Kress et al. have pointed out

that $\chi^{(3)}_{xxxx}$ plays the dominant role, but Bartel et al., have given much credit to $\chi^{(3)}_{xxyy}$. Nevertheless, A. Houard et al., have recently reveals the significant contribution of the cross terms of the optical susceptibility tensor, i.e. $\chi^{(3)}_{yxyx}$. On the other hand, during much study of the EC model, mainly the THz polarization parallel to the fundamental pump beam is investigated. The validity of the EC theory to the orthogonal THz polarization has not been uncovered.

Comprehensive understanding about the physical mechanism is not only essential from the fundamental physical point of view, but also crucial to the coherent control of the THz wave. In the current work, we have experimentally studied the THz power variation as a function of the rotational angle of the BBO crystal, which was put in the path of a focused near-infrared femtosecond laser pulse to generate second harmonic pulse and perform two-color laser field pumping. Comparative study of 4*WM* model and EC model has also been carried out by numerical simulations. The orthogonal THz polarizations have been considered in both the experiments and simulations. It has been found that the outcome given rise by EC model lead to obvious discrepancy with experimental results. However, the 4*WM* model could reproduce the experimental results, indicating a better description to the physical mechanism of THz wave generation by two-color laser field.

2. Experiments

The experimental setup is shown in Fig. 1. A 1 *kHz*, 800 *nm*, 50 *fs* Ti: sapphire laser pulse was spilt into two paths. One was the pump beam and the other was used as the probe of electro-optic sampling (EOS). The energy of the pump beam was about 1 *mJ*/pulse and focused by a f = 175 *mm* lens. The thickness of the inserted type I phase matching BBO crystal was 0.098 *mm*. A plasma was induced by the laser pulse at the focus. And the exiting THz pulse from the plasma was first collimated by an off-axis parabolic mirror (D = 50 *mm*, *f* = 100 *mm*), then focused by another identical parabolic mirror onto a 1 *mm*-thick ZnTe crystal. In addition, a teflon plate, which has high transmission for THz, was put in front of the collimating parabolic mirror to block the laser beams. The probe beam was combined with THz pulse by a Pellicle beam splitter, performing EOS measurement. As indicated by Fig. 2, XYZ is our laboratory coordinate system. The X-axis and the Y-axis are parallel and perpendicular to the pump beam polarization, respectively. The Z-axis is along the laser propagation direction. In order to study the polarization of the THz pulse, two EOS configurations were employed. $E_{THz,X}$ was measured in the first configuration. It is realized by setting a wire grid polarizer between the two parabolic mirrors for high transmission of X polarized THz component. Under this circumstance, the polarization of the probe beam was also parallel to the X-axis. And the (001) axis of the ZnTe crystal was required to be perpendicular to the X-axis of our laboratory coordinate. In contrast, the second configuration was implemented to measure $E_{THz,Y}$. In this case, the wire grid, the probe beam polarization and the ZnTe crystal were rotated 90^o in the XY plane. Weak THz signal generated by the

optical rectification in BBO crystal has been carefully subtracted for both configurations. Furthermore, $E_{THz,X}$ and $E_{THz,Y}$ were measured as a function of the rotation angle of the BBO crystal θ, which was defined as the angle between the X-axis and the extraordinary refractive index axis (e-axis) of the BBO crystal as illustrated by Fig.2, i.e. the angle between the 2ω wave polarization and the X-axis because a type I phase matching BBO crystal was used.

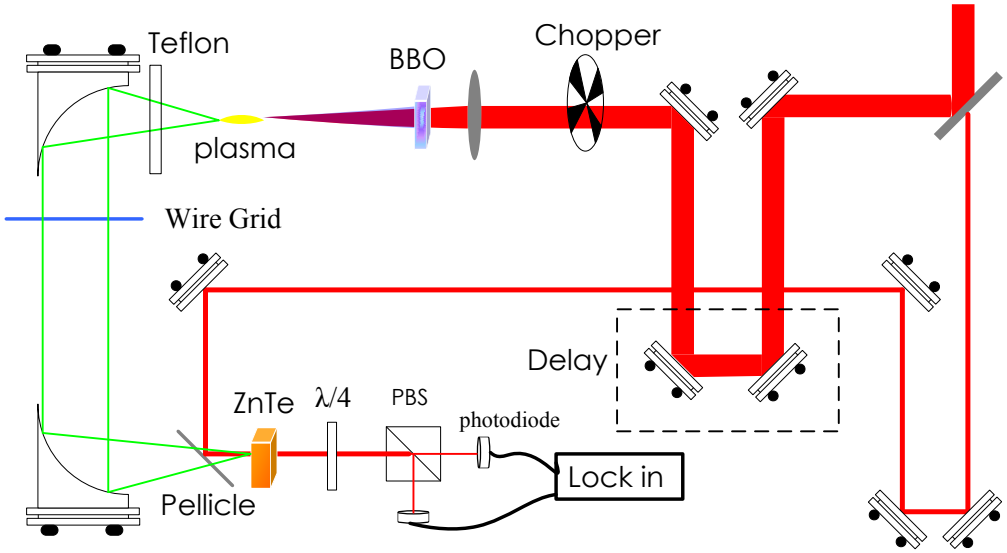

Fig.1 Schematic of the experimental setup.

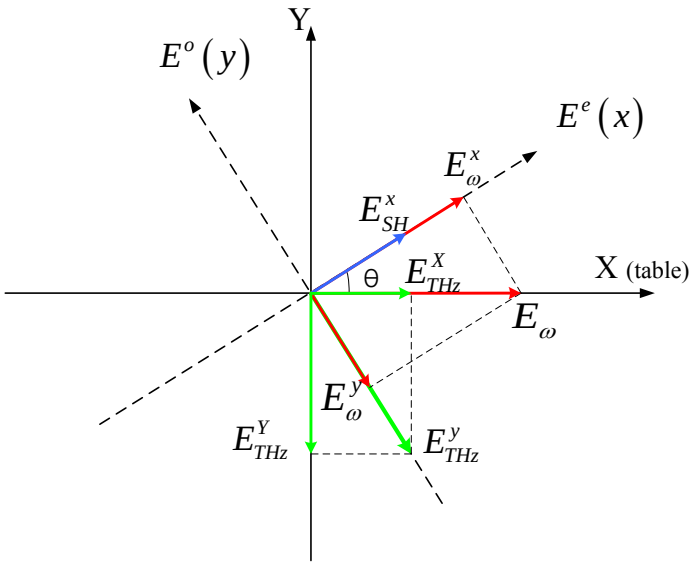

Fig. 2 Coordinate Systems defined in this work.

The experimental results are presented in Fig. 3. When θ is varied, the evolution of the peak to peak amplitudes of $E_{THz,X}$ and $E_{THz,Y}$ are shown as solid circles in Fig. 3(a) and solid triangles in Fig. 3(b), respectively. After two complex components $E_{THz,X}$ and $E_{THz,Y}$ have been acquired for a given θ, it is feasible to retrieve the instantaneous electric field vector by

using $E_{THz} = E_{THz,X}\hat{X} + E_{THz,Y}\hat{Y}$, where $\hat{X}$, $\hat{Y}$ are the unit vectors. It is found that the polarization of the THz wave remains mainly linear and its polarization is mainly perpendicular to that of the second harmonic [9]. Reminding that for a type-I phase-matching BBO crystal, the polarization of 2ω wave is along the e-axis of the crystal, the polarization of the obtained THz wave is mainly parallel to o-axis as indicated in Fig. 2. On the other hand, the THz pulse power I could also be retrieved as

$$I_{THz} = I_{THz,X} + I_{THz,Y} \propto E_{THz,X}^2 + E_{THz,Y}^2, \quad (1)$$

which is shown in Fig. 3(c) as the solid squares. Four maxima could be noticed in Fig. 3(b) at θ = 55°, 118°, 231° and 296° respectively.

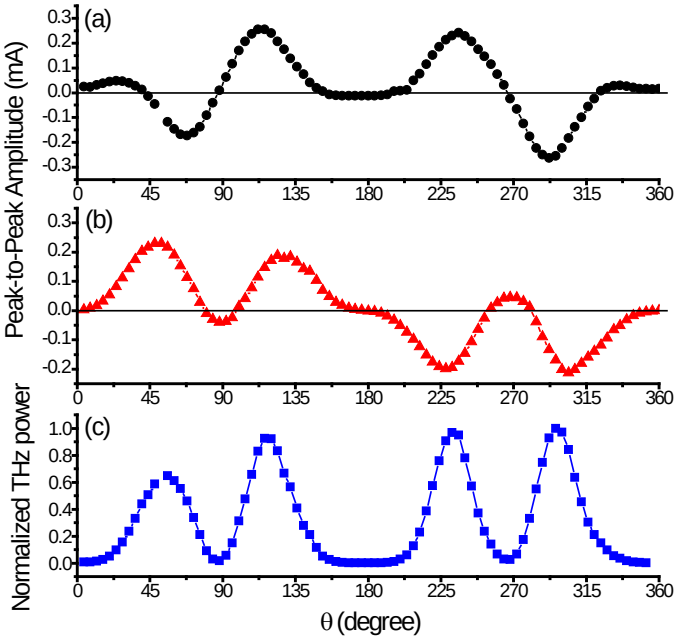

Fig. 3 (a) Variation of $E_{THz,X}$ (open cycles) as a function of θ. (b) The same as (a) for $E_{THz,X}$. (c) Calculated THz power according to Eq. (1).

3. Numeric simulations

3.1 Free electron drifting model

In order to calculate the generated THz energy according to the EC model, the knowledge about the free electron generation dynamic and the temporal distribution of two-color laser filed at focus is essential. For the former, the static tunneling ionization model will be introduced. However for the later, due to the birefringence of BBO crystal and dispersion in

air, the laser field distortion occurred during the propagation prior to the focus has to be taken into account.

3.1.1 Retrieve two-color laser field at focus

The complex laser field at the focus could be decomposed into three parts as the following:

$$\vec{E} = E_{1,\mathrm{o}}\hat{\mathrm{o}} + E_{1,\mathrm{e}}\hat{\mathrm{e}} + E_{2,\mathrm{e}}\hat{\mathrm{o}} \tag{2}$$

where the subscripts 1 and 2 denotes the fundamental light (FL) and the second harmonic light (SH) respectively. The subscripts o and e indicate the polarizations parallel to the ordinary and extraordinary refractive index axis of the BBS crystal, respectively. In the coordinate moving at the group velocity of $E_{1,o}$, $E_{1,o}$, $E_{1,e}$ and $E_{2,e}$ could be expressed as:

$$\begin{aligned}
E_{1,\mathrm{o}}(t) &= E_1(t-\Delta t_1)\sin\theta\cos[\omega_1(t-\Delta t_1) - (n_{1,\mathrm{o}} - n_{g_{1,\mathrm{o}}})\frac{\omega_1}{c}L_1 - (n_{1,a} - n_{g1,a})\frac{\omega_1}{c}L_2] \\
E_{1,\mathrm{e}}(t) &= E_1(t)\cos\theta\cos[\omega_1 t - (n_{1,\mathrm{e}} - n_{g_{1,\mathrm{e}}})\frac{\omega_1}{c}L_1 - (n_{1,a} - n_{g_{1,a}})\frac{\omega_1}{c}L_2] \\
E_{2,\mathrm{e}}(t) &= \beta E_1^2(t-\Delta t_2)\sin^2\theta\cos[\omega_2(t-\Delta t_2) - (n_{2,\mathrm{e}} - n_{g_{2,\mathrm{e}}})\frac{\omega_2}{c}L_1 - (n_{2,a} - n_{g2,a})\frac{\omega_2}{c}L_2 + \frac{\pi}{2}]
\end{aligned} \tag{3}$$

where β is a proportional factor. Δt_1 and Δt_2 accounts for the group delays of $E_{1,o}$ and $E_{2,e}$ in BBO crystal and air, respectively. They are given by

$$\begin{aligned}
\Delta t_1 &= \frac{L_1}{c}(n_{g1,o} - n_{g1,e}) \\
\Delta t_2 &= \frac{L_2}{c}(n_{g2,a} - n_{g1,a})
\end{aligned} \tag{4}$$

Note that inside the BBO crystal, the group delay between the SH pulse and the *e* polarized FL leads to the pulse broadening of the SH pulse. Therefore, it could be included by revising the analytic expression for $E_{2,o}(t)$ as the following:

$$E_{2,\mathrm{e}}(t) = E_2(t-\Delta t_2)\sin^2\theta\cos[\omega_2(t-\Delta t_2) - (n_{2,\mathrm{e}} - n_{g_{2,\mathrm{e}}})\frac{\omega_2}{c}L_1 - (n_{2,a} - n_{g2,a})\frac{\omega_2}{c}L_2 + \frac{\pi}{2}] \tag{5}$$

where $E_2(t-\Delta t_2)$ denotes the envelope function of the second harmonic pulse which is Gaussian like. Eq. (3) and (5) also consider the carrier envelop phase evolving due to a difference between the phase velocity and the group velocity. The meanings of the symbols appeared in Eq. (3)~(5) and their values are listed in Tab. 1.

In order to derive the refractive indices and group indices listed in Tab. 1, the following Sellmeier equations have been implemented :

in BBO crystal [10]:
$$\begin{aligned} n_o^2 &= 2.7405 + \frac{0.0184}{\lambda^2 - 0.0179} - 0.0155\lambda^2 \\ n_e^2 &= 2.3730 + \frac{0.0128}{\lambda^2 - 0.0156} - 0.0044\lambda^2 \end{aligned}, \quad (6)$$

and in air [11]:
$$(n_a - 1)\times 10^8 = 8342.1 + \frac{2406030\lambda^2}{130\lambda^2 - 1} + \frac{15996\lambda^2}{38.9\lambda^2 - 1}. \quad (7)$$

Symbol	Description	Value	Units
ω_1	angular frequency of FL	2.36	fs^{-1}
ω_2	angular frequency of SH	4.71	fs^{-1}
$n_{1,o}$	ordinary refractive index of FL in BBO crystal	1.661372095	
$n_{1,e}$	extraordinary refractive index of FL in BBO crystal	1.633818527	
$n_{2,e}$	extraordinary refractive index of SH in BBO crystal	1.670195247	
$n_{1,a}$	refractive index of FL in air	1.000275036	
$n_{2,a}$	refractive index of SH in air	1.000282747	
$n_{g1,o}$	ordinary group index of FL in BBO crystal	1.685658213	
$n_{g1,e}$	extraordinary group index of FL in BBO crystal	1.660100295	
$n_{g2,e}$	extraordinary group index of SH in BBO crystal	1.770512998	
$n_{g1,a}$	group index of FL in air	1.000279952	
$n_{g2,a}$	group index of SH in air	1.000304262	
L_1	thickness of BBO crystal	98	μm
L_2	distance from the back surface of BBO crystal to the focus	5	cm

Tab. 1 List of experimental parameters

For a BBO crystal cut at a angle α (= 29.8° in our experiment), the extraordinary refractive index of a normally incident light is obtained by

$$\frac{1}{n_e^2(\alpha)} = \frac{\cos^2\alpha}{n_o^2} + \frac{\sin^2\alpha}{n_e^2} \quad (8)$$

By substituting all the experimental parameters into Eq.(3)~(5), we could reconstruct the temporal laser field distribution at the focus. The resulted $E_o = E_{1,o}$ and $E_e = E_{1,e} + E_{2,e}$ are plotted in Fig. 4 for $\theta = 55^o$ as an example. Here, the pulse duration of the SH pulse has been assumed to be the same as FL, i.e., 50 *fs*. In practice, we have found that the pulse duration of SH does not play significant role in our simulation. It can be understood since in the EC model, THz radiation is induced by the asymmetric electric field distribution and has little relevant to the field envelope [6]. The asymmetry of E_e induced by the combination of $E_{1,e}$ and $E_{2,e}$ could be clearly seen in Fig. 4.

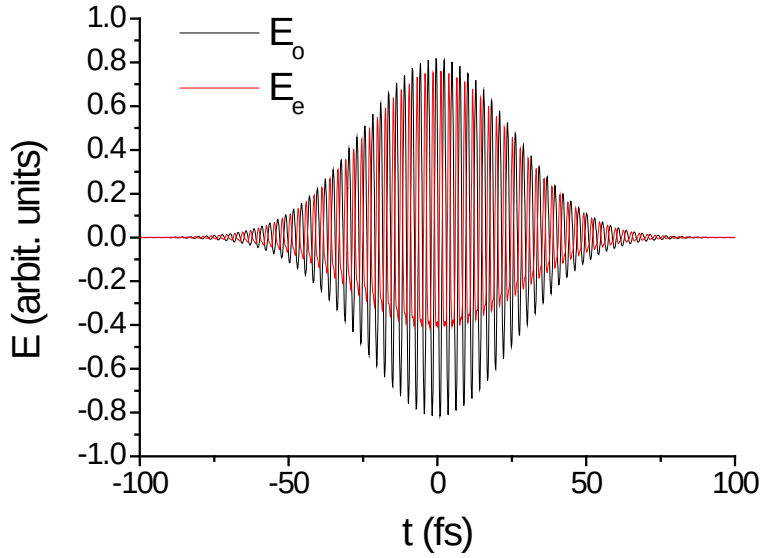

Fig. 4 The resulted $E_o = E_{1,o}$ (black line) and $E_e = E_{1,e} + E_{2,e}$ (red line) for $\theta = 55^o$ as an example.

3.1.2 Simulate free electron generation rate

In our experiment, tunneling ionization dominates the free electron generation process. The ionization rate R(t) could be commonly described by the static tunneling model in the form of [6].

$$R(t) = \frac{a}{A(t)} \exp(-\frac{b}{A(t)}) \tag{9}$$

where $A(t) = \left|\vec{E}(t)\right| / E_a$ is the electric field in atomic units and

$$
\begin{aligned}
&E_a = \kappa^3 m^2 e^5 / \hbar^4 \approx 5.14 \times 10^{11}\ \mathrm{V/m} \\
&a = 4\omega_a r_H^{5/2} \\
&b = (2/3) r^{3/2} \\
&\omega_a = \kappa^2 m e^4 / \hbar^3 \approx 4.16 \times 10^{16}\ \mathrm{/s}
\end{aligned}
\tag{10}
$$

ω_a corresponds to the atomic frequency unit, $r_H = U_{ion}/U_H$ indicates the ionization potential of the gas molecules under consideration relative to that of hydrogen(U_H = 13.6 *eV*) and $\kappa = (4\pi\varepsilon_0)^{-1}$. In the simulations, the air is considered as being composed of 78 % nitrogen and 22% oxygen with $U_{ion,\,N2}$ = 15.6 *eV* and $U_{ion,\,O2}$ = 12.1 *eV*. Hence, the electron density $N_e(t)$ is given by:

$$
\begin{aligned}
&dN_e(t) = dN_e(t)_{N_2} + dN_e(t)_{O_2} \\
&dN_e(t)_{N_2} = R(t)_{N_2}[N_{0N_2} - N_e(t)_{N_2}]dt \\
&dN_e(t)_{O_2} = R(t)_{O_2}[N_{0O_2} - N_e(t)_{O_2}]dt
\end{aligned}
\tag{11}
$$

Since the laser intensity at the focus is not precisely known, it is assumed that the peak amplitude of E_1 in Eq. (3) is 2×10^8 *V/cm*, corresponding to a laser intensity of 1×10^{14} *W/cm*^{2} at the focus [3]. The peak amplitude of E_2 in Eq. (5) is assumed to be 0.6×10^8 *V/cm*. In Fig. 5, we demonstrate the calculated $dN_e(t)$ and $N_e(t)$ induced by the laser field shown in Fig. 4.

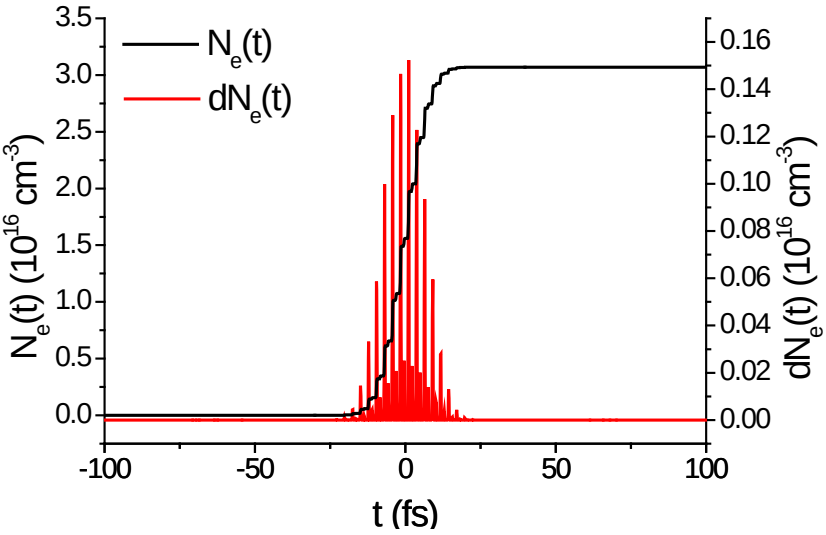

Fig. 5 Calculated free electron density $dN_e(t)$ and $N_e(t)$ are shown as the red line and blue line, respectively.

It is important to point out that we have carefully verified that the ionization dynamic is not sensitive to the peak amplitude of E_1 as long as the ionization probability is beyond the saturation region where depletion of the neutral molecules takes place. It is fulfilled in our experiment since Fig. 5 implies that the maximum ionization probability is in the order of 1‰. However, the ratio between the amplitudes of E_1 and E_2 plays crucial role. In order to determine this ratio, another experiment has been carried out.

In details, perpendicular to the propagation axis, the fluorescence light emitted from the plasma column was collected by a 1-*inch*-diameter fused silica lens, whose focal length was 1 *inch*, onto a photomultiplier tube (PMT). In front of PMT, an interference filter was inset to isolate one particular nitrogen fluorescence spectral line, namely, the (1-0) vibronic transition of the second positive band system of N_2 at 357*nm*, from the scattered light of the pump beam. Then the PMT signal was sent to an oscilloscope for analysis. The strength of the fluorescence signal was recorded as a function of the BBO crystal rotational angle θ. We have known that the registered fluorescence signal is a good indication of the free electron density [12]. The experimental measurement is depicted in Fig. 6 as the black circles. Best fitting of the simulation results could be found when the ratio is set to be 0.3 shown as the red line in Fig. 6.

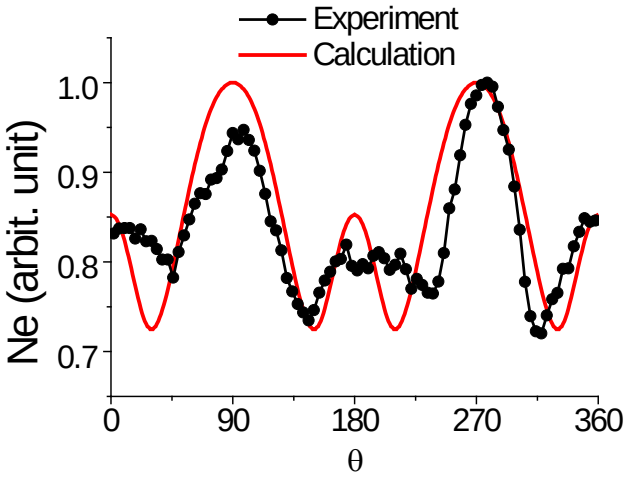

Fig. 6 Normalized free electron density as a function of the BBO crystal angle θ. Black circles: experimental measurement; red line: simulation.

3.1.3 Calculate net free electron drifting current

With the electron density $N_e(t)$ obtained from the ionization rate, the electron drifting current J(t) can be computed as

$$J(t) = \int_{-\infty}^{t} N_e(t_0) v(t_0) dt_0 \tag{12}$$

where $v(t_0)$ denotes the electron velocity under the laser field given by

$$v(t;t_0) = -\frac{e}{m}\int_{t_0}^{t} E(t')dt' \tag{13}$$

The THz pulse amplitude is determined by the net free electron drifting current J(t) after the laser pulse is gone. The corresponding net free electron drifting current as a funcation of θ is shown in Fig. 7 for both the polarization parallel to o-axis (panel (a)) and e-axis (panel (b)) of the BBO crystal, respectively. Fig. 7(b) hints that according to the EC model, there is

significant THz wave generation whose polarization is along the e-axis of the BBO crystal. However, it is not the case in our experiment as we have mentioned previously.

In fact, different second harmonic field peak amplitudes have been attempted in our computation. None of them could reproduce the experimental results shown in Fig. 3 and Fig. 6. Fig. 8 demonstrates two examples when the second harmonic field strength is set to be 0.2×10^8 *V/cm* and 1×10^8 *V/cm* Based on the results we have obtained so far, it seems that only the free electron drifting model has difficulty in explaining our experimental results.

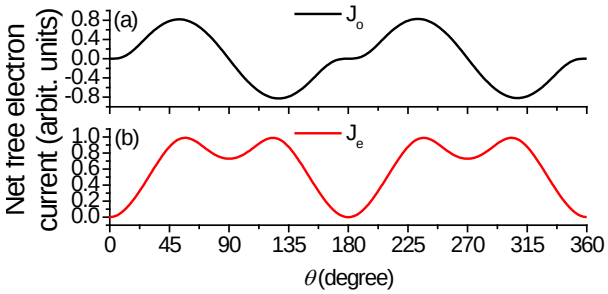

Fig. 7 Calculated net free electron drifting current in the directions parallel to the o-axis ((a)) and e-axis ((b)) of the BBO crystal, respectively.

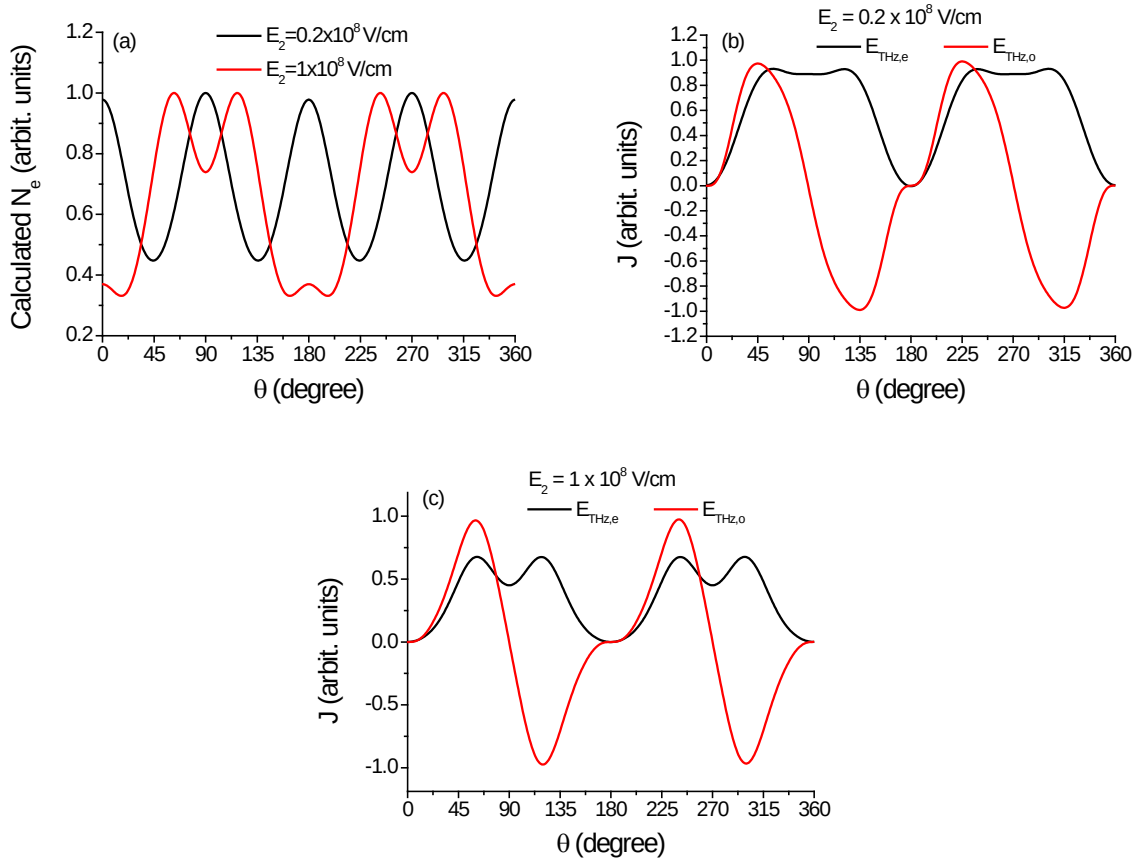

Fig. 8 Calculated θ dependent (a) free electron density for $E_2 = 0.2\times10^8$ *V/cm* and $E_2 = 1\times10^8$ *V/cm*; (b) net free electron drifting current when $E_2 = 0.2\times10^8$ *V/cm*; (c) net free electron drifting current when $E_2 = 1\times10^8$ *V/cm*.

4. Four wave mixing model

Here, for the sake of convenience, we still use the BBO crystal coordinate system – oez. The z-axis still points to the propagation direction. Thus, the electric fields of the second harmonic and THz are denoted in the new coordinate system by $E_{2,e}$ and $E_{THz,o}$, respectively. However, the electric field of the input pump beam will have two complex components $E_{1,o}$ and $E_{1,e}$ with relative phase shift induced by the birefringence of the crystal. These coordinates are sketched in Fig. 2. The four-wave mixing model gives:

$$E_{THz,i} \propto \sum_{jkl} \chi^{(3)}_{ijkl} E_{2,j} E_{1,k} E_{1,l} \quad (i,\ j,\ k,\ l = o,\ e) \tag{14}$$

In Eq. (14), the phase term has been dropped since it is constant in principle. Note that the polarization of THz is mostly perpendicular to that of the second harmonic wave Taking into account that only $E_{2,e}$ is present and $E_{THz,o}$ is the dominant THz filed polarization component, we need to consider the simplified form of Eq. (1):

$$E_{THz,o} \propto \sum_{jkl} \chi^{(3)}_{oekl} E_{2,e} E_{1,k} E_{1,l} \qquad (k,\ l = o,\ o) \tag{15}$$

Recalling that in a centrosymmetric optical media such as air, $\chi^{(3)}_{oeoo} = \chi^{(3)}_{oeee} = 0$ and $\chi^{(3)}_{oeoe} = \chi^{(3)}_{oeeo}$, we finally get:

$$E_{THz,o} \propto \chi^{(3)}_{oeoe} E_{2,e} E_{1,o} E_{1,e} \tag{16}$$

According to the vectorial diagram described in Fig. (2), we substitute $E_{1,e} \propto E_1 \cos\theta$, $E_{1,o} \propto -E_1 \sin\theta$ and $E_{2,e} \propto (E_1 \sin\theta)^2$ into Eq. (16), giving rise to:

$$E_{THz,o} = -dE_1^4 \sin^3\theta \cos\theta \tag{17}$$

where d is a proportionality factor which already takes into account $\chi^{(3)}_{oeoe}$. Further projection of $E_{THz,o}$ onto X, Y axis leads to:

$$\begin{aligned} E_{THz,X} &= E_{THz,o} \cos(\theta - 90^o) = -aE_1^4 \sin^3\theta \cos\theta \cos(\theta - 90^o) \\ E_{THz,Y} &= E_{THz,o} \sin(\theta - 90^o) = -aE_1^4 \sin^3\theta \cos\theta \sin(\theta - 90^o) \end{aligned} \tag{18}$$

The computation results are indicated in Fig. 9. The outcome follow closely the

measurement data shown in Fig. 3. Therefore, through two dimensional THz polarization study, we have clearly demonstrates the dominant role of $\chi^{(3)}_{yxyx}$ (equivalently, $\chi^{(3)}_{yxxy}$) in the framework of 4*WM* model, as compared to the rest susceptibility tensor elements.

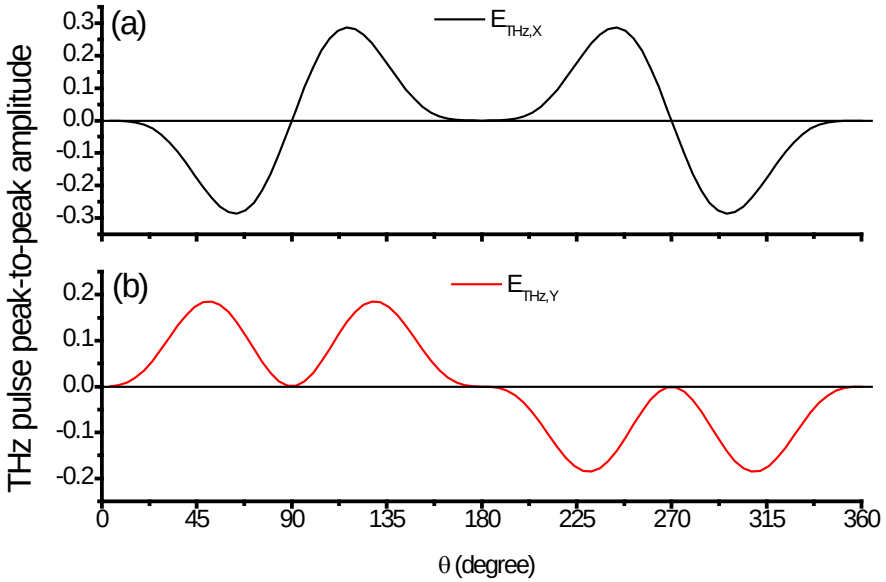

Fig. 9 Calculated peak amplitudes of $E_{THz,X}$ and $E_{THz,Y}$ as a function of θ according to the 4*WM* model.

5. Conclusions

In summary, by using an EOS technique, we measured the two vectorial components of the THz wave generated by two-color laser field in air plasma. One polarization of the THz wave is parallel to the input fundamental laser polarization, and the other is perpendicular to the input fundamental laser polarization. In order to shed further light onto the physical mechanism of this interesting nonlinear optical process, comparison study has been performed between the free electron drifting current model and the macroscopic four-wave mixing model theoretically. The simulation results indicate that the four-wave mixing model could successfully reproduce our experimental observations. While the calculation outcome given rise by the free electron drifting current model show obvious discrepancy with our experimental results. Therefore, we conclude that four-wave mixing model could be a more comprehensive theoretical model than the free electron drifting current model to interpret the physical dynamic during the THz generation by two-color laser field in gas medium.

Acknowledgment

The authors acknowledges the support of the 973 Program (grant No.2007CB310403.), NSFC (grants No. 10804056), NCET, SRFDP, Fok Ying Tong Education foundation, the open

fund of the State Key Laboratory of High field Laser Physics (SIOM) and SRF for ROCS, SEM. SLC acknowledges the support of Canada Research Chair and NSERC.

References

[1] T. Bartel, P. Gaal, K. Reimann, M. Woerner, and T. Elsaesser, "Generation of single-cycle THz transients with high electric-field amplitudes", *Opt. Lett.* 30, 2805-2807, (2005).

[2] M. Kress, T. Loffler, S. Eden, M.Thomson, and H. G. Roskos, "Terahertz-pulse generation by photoionization of airwith laser pulses composed of both fundamental and second-harmonicwaves", *Opt. Lett.* 29, 1120-1122, (2004).

[3] K. Y. Kim, A. J. Taylor, J. H. Glownia, and G. Rodriguez, "Coherent control of terahertz supercontinuum generation in ultrafast laser–gas interactions", *Nat. Photon.* 2, 605, (2008).

[4] X. Xie, J. M. Dai, and X. C. Zhang, "Coherent control of THz wave generation in ambient air", *Physical Review Letters* 96, 075005, (2006).

[5] A. Houard, Y. Liu, B. Prade, and A. Mysyrowicz, "Polarization analysis of terahertz radiation generated by four-wave mixing in air", *Opt. Lett.* 33, 1195, (2008).

[6] M. D. Thomson, M. Kress, T. Loffler, and H.G. Roskos, "Broadband THz emission from gas plasmas induced by femtosecond optical pulses: From fundamentals to applications", *Laser & Photonics Rev.* 1, 349, (2007).

[7] H. Hamster, A. Sullivan, S. Gordon, W. White, and R. W. Falcone, "Subpicosecond, electromagnetic pulses from intense laser-plasma interaction", *Physical Review Letters* 71, 2725-2728, (1993).

[8] Y. Zhang, Y. Chen, C. Marceau, W. Liu, Z.-D. Sun, S. Xu, F. Théberge, M. Châteauneuf, J. Dubois, and S. L. Chin, "Non-radially polarized THz pulse emitted from femtosecond laser filament in air", *Optics Express* 16, 15483-15488, (2008).

[9] Y. Zhang, Y. Chen, S. Xu, H. Lian, M. Wang, W. Liu, S. L. Chin, and G. Mu, "Portraying polarization state of terahertz pulse generated by a two-color laser field in air", *Opt. Lett.* 34, 2841-2843, (2009).

[10] *Handbook of Optics,* Vol. 2, 2nd edition. McGraw-Hill, (1994).

[11] Warren J. Smith, *Modern Optical Engineering*, 3rd edition. McGraw-Hill, (2000).

[12] S. Xu, Y. Zhang, W. Liu, S. L. Chin, "Experimental confirmation of high-stability of fluorescence in a femtosecond laser filament in air", *Optics Communications* 282, 4800–4804, (2009).